Provided for non-commercial research and education use.
Not for reproduction, distribution or commercial use.

Volume 65, issue 8, October 2011

ISSN 1359-6462

ELSEVIER

Scripta MATERIALIA

A LETTERS JOURNAL

STRUCTURE
PROPERTIES
THEORY
PROCESSING
FUNCTION

Available online at SciVerse ScienceDirect www.sciencedirect.com

www.elsevier.com/locate/scriptamat

This article appeared in a journal published by Elsevier. The attached copy is furnished to the author for internal non-commercial research and education use, including for instruction at the authors institution and sharing with colleagues.

Other uses, including reproduction and distribution, or selling or licensing copies, or posting to personal, institutional or third party websites are prohibited.

In most cases authors are permitted to post their version of the article (e.g. in Word or Tex form) to their personal website or institutional repository. Authors requiring further information regarding Elsevier's archiving and manuscript policies are encouraged to visit:

http://www.elsevier.com/copyright

Available online at www.sciencedirect.com

ScienceDirect

Scripta Materialia 65 (2011) 695–698

Scripta MATERIALIA

www.elsevier.com/locate/scriptamat

Tension behavior of free-standing amorphous film and amorphous–crystalline nanolaminates in submicron scale

C.J. Lee,[a,*] H.K. Lin,[b,c] J.C. Huang[a] and S.Y. Kuan[a]

[a] *Department of Materials and Optoelectronic Science, Center for Nanoscience and Nanotechnology, National Sun Yat-Sen University, Kaohsiung 804, Taiwan*

[b] *Laser Application Technology Center/Industrial Technology Research Institute South (ITRI South), Liujua Shiang 734, Taiwan*

[c] *China Steel Corporation, Kaohsiung 812, Taiwan*

Received 23 February 2011; revised 5 July 2011; accepted 7 July 2011
Available online 14 July 2011

Free-standing amorphous ZrCu film and amorphous–crystalline ZrCu/Cu nanolaminates are subjected to membrane deflection experiments to investigate their tensile deformation. The ZrCu specimen exhibits poor deformability with brittle fracture. In comparison, moderate plasticity occurs for the nanolaminates, and the plasticity increases as the thickness of the individual layers decreases from 100 down to 25 nm. The ZrCu/Cu nanolaminates with a layer thickness of 25 nm exhibit a fracture angle close to 45° and a dimpled fracture surface, implying moderate tensile ductile fracture.

© 2011 Acta Materialia Inc. Published by Elsevier Ltd. All rights reserved.

Keywords: Tensile deformation; Amorphous thin film; Free-standing film; Nanolaminate; Multilayer

---

Improving the ductility of metallic glasses (MGs) has always been a critical issue. Proposed approaches for improving plasticity include the concept of intrinsic [1–5] or extrinsic [6–8] metallic glass composites (MGCs), as well as nano- and microscaled phase separation [9,10]. For monolithic MGs or MGCs, compressive plasticity has been demonstrated by a large number of studies. There have been fewer studies, however, on tensile ductility, where the initial cracking of shear bands is confined throughout the entire tensile specimens, so that they exhibit plasticity beyond the elastic limit. It has been suggested that some soft crystalline precipitates introduced into the MG matrix are responsible for this, and that the spacing (or length scale) between such crystalline obstacles is an important parameter for the plastic shielding of an opening crack tip to limit the extension of the shear band.

Nanolaminate structures of crystalline materials can be used to study the characteristics of nanocrystalline materials [11], and these amorphous–crystalline multilayers or nanolaminates are also feasible routes by which to improve the MG plasticity, especially under tensile deformation. Nieh et al. [12] and Wang et al. [13] synthesized amorphous CuZr (5 nm thick)/crystalline Cu (35 nm thick) nanolaminates via sputter processing. The nanolaminates exhibited outstanding tensile ductility (10–15% strain) at room temperature and a high strength of ~1.1 GPa. Also, the amorphous PdSi (10 nm thick)/crystalline Cu (90 nm thick) nanolaminates fabricated by Donohue et al. [14] could be rolled to a 60–80% thickness reduction without fracture or formation of major fatal shear bands. These aforementioned amorphous–crystalline nanolaminates possessing thin amorphous layers (typically thinner than the ~25 nm width of the shear band) and sufficiently thick and stiff crystalline layers can suppress the formation of principal shear bands, giving them superior ductility. However, in the previously reported cases, the crystalline layers occupy an overall volume fraction greater than 80%. These nanolaminates should thus be termed as crystalline-base composites, rather than metallic glass composites. It is of interest to see if nanolaminates with an amorphous phase volume fraction of 50% or above can still show good tensile ductility. It is important to ascertain whether such outstanding plasticity can be retained under tensile deformation.

For most reported studies on film tension [15–17], the facile measurement of tensile deformation for the thin film materials was conducted directly by coated uniaxial tensile specimens with a polymer or silicon substrate. Another method is to perform a bending test and

---

[*] Corresponding author. Tel.: +886 7 5254070; fax: +886 7 5254099; e-mail: leechingjen@gmail.com

1359-6462/$ - see front matter © 2011 Acta Materialia Inc. Published by Elsevier Ltd. All rights reserved.
doi:10.1016/j.scriptamat.2011.07.015

examine the tension-side deformation [18]. Nevertheless, the interface properties between the substrate and the film would influence the mechanical behavior of the coated films during deformation [15,16,19,20]. In the literature, a number of tensile testing designs have been developed for free-standing films, including the bulge test [21,22], microbeam bending [21,22] and the membrane deflection test [23]. In this study, the membrane deflection method is employed to study free-standing and amorphous–crystalline nanolaminates with various layer thicknesses.

(1 0 0) Si wafers that had undergone double-sided polishing were first covered on both sides with a layer of ~550 nm Si_3N_4 film, deposited by low-pressure chemical vapor deposition, to act as a protective membrane during the subsequent wet etching of the wafers. Some portions of the Si_3N_4 layer were removed with a pulsed ultraviolet laser on the bottom side of Si wafer to form a pattern of etching windows. The pre-processed Si wafers were cleaned in an ultrasonic cleaner for 5 min with deionized water, ethanol and acetone, then dried with nitrogen gas. After the cleaning process, the ZrCu amorphous layers and Cu nanocrystalline layers were deposited sequentially onto the top side of each pre-processed Si wafer. The volume fraction of ZrCu and Cu was fixed to 50%. Samples with ZrCu/Cu thickness of 100/100, 50/50 and 25/25 nm, and a monolithic ZrCu layer – referred to as ZCC-100, ZCC-50, ZCC-25, and ZC, respectively – were fabricated, and the overall thickness of the ZrCu/Cu nanolaminates was kept at about 1 μm. Wet etching in 40% KOH solution and dry etching in CF_4 and O_2 plasma were utilized to remove the Si substrate and Si_3N_4 layer below the ZrCu/Cu nanolaminates, respectively.

The free-standing nanolaminates were subsequently machined to form a dogbone-shaped bridge specimen with a focused ion beam (FIB). The half length of the bridge span, the gage length of the dogbone-shaped specimen and the width of bridge were about 65–75, 40–50 and 7 μm, respectively. A Berkovich tip was indented onto the central part of the dogbone-shaped bridge specimen to induce tensile deformation in an MTS XP nanoindenter. The method used followed the membrane deflection experiment [24]. The loading rate control mode of the basic mode was adopted during the indentation. The loading rate and maximum load were 5×10^{-3} mN s^{-1} and 5 mN, respectively. The fracture morphology was characterized by scanning electron microscopy (SEM), and the laminated structures of the as-deposited and deformed samples we examined by transmission electron microscopy (TEM).

Figure 1 shows the typically dogbone-shaped bridge specimens for ZCC-100 and ZCC-25 before and after indentation. Due to the residual stress of the as-deposited films, the free-standing membrane dogbone-shaped specimens are typically bent very slightly in the as-FIB-machined condition.

The dogbone-shaped specimens were all loaded by the indenter, and the free-standing membrane underwent tensile deformation until failure. Figure 2 shows the raw curves of load (p)–displacement (h) data. The curves of ZC, ZCC-100 and ZCC-50 all have an inverted L shape, with a lower slope in stage I and a higher slope in stage II, as shown clearly in the inset of Figure 2. In contrast, ZCC-25 does not show this shape, exhibiting a near-power-law curve. In order to simplify the description of the inverted L shape, these curves for stages I and II were fitted by linear lines, and their extracted slopes are listed in Table 1.

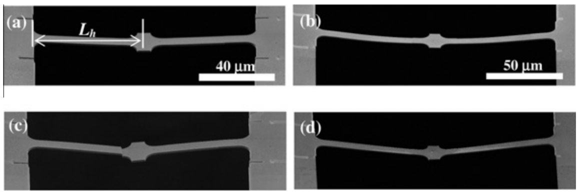

Figure 1. SEM micrographs showing the dogbone-shaped bridge specimens of ZCC-100 and ZCC-25: (a and b) before indentation and (c and d) after indentation, respectively.

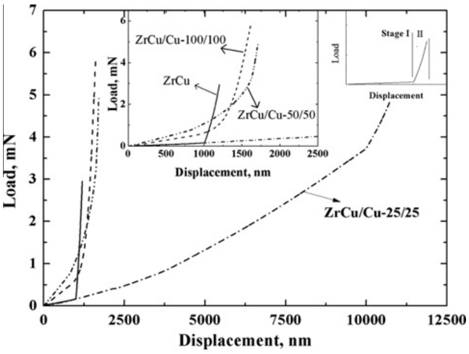

Figure 2. Raw load–displacement curves of the membrane deflection experiment for the ZC, ZCC-100, ZCC-50 and ZCC-25 specimens.

Table 1. Comparison of the slopes, deformability index and fracture stress of the four different free-standing specimens.

	ZC	ZC-100	ZC-50	ZC-25
Stage I slope ($mN\ nm^{-1}$)	1.5×10^{-4}	6.1×10^{-4}	9.3×10^{-4}	–
Stage II slope ($mN\ nm^{-1}$)	0.015	0.016	0.020	–
Deformability index (%)	1.4	2.2	2.4	>15
Fracture stress (GPa)	0.6	2.0	2.5	2.5

These inverted L curves imply that the bridges were subjected to a tensile force on two sides of the indenter for stage I. With increasing indentation force, one side of the bridge would eventually break, resulting in a change of deformation mode from tensile deformation on two sides (stage I) to bending deformation of the one remaining side without breaking (stage II). Due to this change in deformation mode, the specimen stiffness would exhibit the sudden inflection. Note that the stage II slopes of the ZC, ZCC-100 and ZCC-50 specimens in Figure 2 are all nearly identical. Moreover, another phenomenon noted is that the slope of stage I gradually increased from ZC to ZCC-100 to ZCC-50, implying that the hardening rate during tensile deformation increased with decreasing layer thickness for layer thicknesses greater than 50 nm.

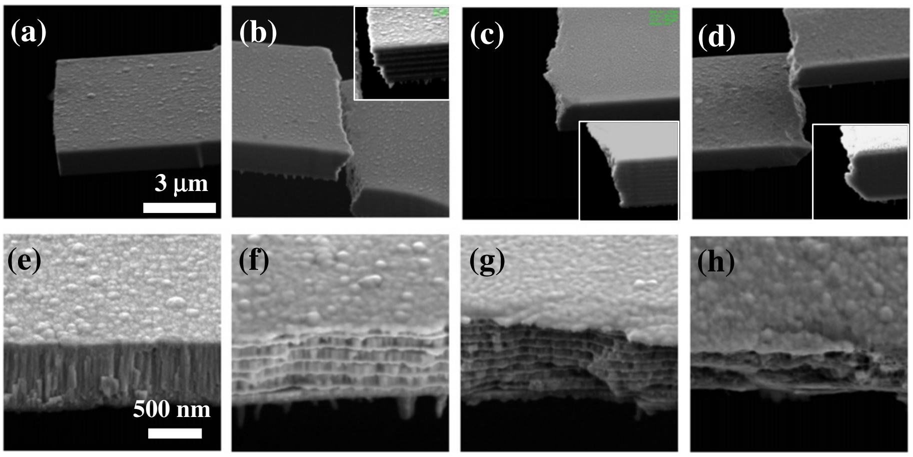

Figure 3. SEM micrographs showing the side views of the fractured specimens: (a and b) ZC, (c and d) ZCC-100, (e and f) ZCC-50 and (g and h) ZCC-25. The insets show enlarged cross-sectional images produced via etching by a lower-current ion beam.

The ZCC-25 specimen, which did not exhibit the apparent inverted L response, could be indented to a depth of ∼11 μm without breaking under an applied indenting load of 5 mN, implying that this specimen has better deformability, as shown in Figure 1(d). In order to break this more ductile ZCC-25 specimen, an even higher load of 7 mN is needed. Due to the difficulty in measuring the true strain within the gage length, we define here a simple deformability index as the indented depth of stage I divided by the half length (L_h, as shown in Fig. 1(a) for a one-wing bridge), and the data are listed in Table 1. The deformability index shows only a slight improvement, from 1.4% to 2.4%, with decreasing layer thickness from the ZC to ZCC-100 to ZCC-50 specimens. However, this index is greatly improved to above 15% when the layer thickness is reduced to 25 nm, i.e. the ZCC-25 specimen. The tensile fracture stress of these dogbone-shaped specimens can be calculated by dividing the membrane load (p_m), which can be calculated from the trigonometric function of the indenter load (p), by the cross-sectional area, as also listed in Table 1. The ZC specimen exhibits a very low tensile fracture stress of 600 MPa, much lower than the typical compressive stress of the binary ZrCu bulk metallic glasses (BMGs) or micropillars (1000–1600 MPa). However, other ZrCu/Cu nanolaminates possess much higher fracture strengths of 2000–2500 MPa.

Figure 3 shows the side views of the specimens after failure, and the insets in Figure 3(b)–(d) are enlarged cross-sectional images obtained via etching by a lower-current ion beam. The fracture angle of the monolithic amorphous ZC specimen in Figure 3(a) is nearly 90°, which is different from the tensile fracture angle (50–56°) for bulk metallic glasses. The fracture proceeds along a nearly straight plane, analogous to that cut by a knife and characteristic of brittle fracture. Observing the fracture plane of ZC from another direction, as shown in Figure 3(e), the fractography exhibits a granular structure without the typical vein-like pattern of the bulk metallic glass samples [24].

Unlike the 90° angle in the monolithic amorphous ZC specimen, the fracture planes of the amorphous–crystalline nanolaminates show an angle of 65–45° between the fracture planes and tensile direction, these angles gradually approaching ∼45° with decreasing layer thickness down to 25 nm (compare Fig. 3(b), (c) and (d)). From the side view, the fracture planes of these nanolaminates also show a zigzag fracture surface, unlike the straight fracture surface of the ZC specimen. The surface zigzagged to a greater degree with decreasing layer thickness, which implies the gradual transformation into a more ductile fracture, consistent with the deformability index in Table 1, especially for the ZC-25 specimen. The fractographs of the multilayer nanolaminates show that the ductile Cu layer seems to be pulled out somewhat with a reduced Cu layer thickness (compare Fig. 3(f), (g) and (h)). Due to the fine structure of the ZCC-25 specimen, the multilayer structure is not very clear under SEM, and its fractography shows a dimple-like characteristic, as shown in Figure 3(h).

Mayr and Samwer [25] found that amorphous thin films, fabricated via evaporation or sputtering, possessed an intrinsic tensile stress, which originated from the balance of hydrostatic pressure during the coalescence of individual small clusters during deposition, dependent on the surface topography and the radius of individual surface cluster. These higher stress concentrations occurred in valleys or at triple points between surface clusters. For this reason, the current ZC amorphous 1 μm film is prone to brittle failure, exhibiting the lower tensile fracture strength of 600 MPa and poor deformability, with the exposure of individual granular clusters on the fracture surface. The thin film metallic glass fabricated by sputtering would have an inherent granular structure, residual tensile stress and an inevitably brittle nature. How to anneal or decrease the residual tensile stress is a subject worthy of future study.

For amorphous–crystalline nanolaminates, when considering the deformation mechanism, the basic mechanism of shear bands or shear transformation zones (STZs) for the amorphous layers and dislocations and/or twins for the nanocrystalline layers should be considered, as well as the interface interaction between the amorphous and crystalline layers. Misra et al. [26] mentioned the dependence of the dislocation mechanism on the layer thicknesses of the crystalline multilayers. As the layer thickness becomes greater than the submicron scale, dislocation pile-ups could occur. In contrast, as the layer thickness falls to the range of a few nanometers to a few tens of nanometers, dislocations would be confined to slip in the individual layers due to the geometric and repulsive effects. In parallel, the nucleation and propagation of shear bands in the amorphous layers would also need sufficient space. Recent studies [27,28] have proposed a length scale comparable to the width of a shear band (about 20–50 nm) as the critical boundary. As the specimen's dimensions are smaller than or equal to this critical width, the basic deformation unit, the STZ, would be unlikely to form into major shear bands, resulting in homogeneous-like deformation in the metallic glass.

A crystalline Cu layer of 100 or 50 nm thickness would have an enough capacity for dislocation pile ups, which generate high stress concentrations in the interface between the crystalline and amorphous layers. These points of stress concentration would readily induce the formation of shear bands (or microcracks) along the granular boundaries owing to the intrinsic tensile stress of the amorphous ZrCu film, making the fractography of the ZrCu layers similar to that of the ZC specimen, as shown in Figure 3(f) and (g). In addition, the Cu thickness after failure is smaller than the ZrCu thickness near the fracture end, as shown in Figure 3(f) and (g), implying that the Cu layers have been pulled out to cause the necking phenomenon in the fracture plane. This necking phenomenon also indirectly implies that the Cu layer fractures after the ZrCu layers, which could explain the zigzag fracture surface resulting from the ductile Cu layer obstructing the propagation of the shear bands (or microcracks) to change the direction of the crack. This would enable the ZCC-100 and ZCC-50 specimens to possess better tensile ductility than the monolithic ZC specimen.

For the 25 nm Cu layers, the dislocation motion becomes a confined layer slip without any pile up [26]. This change not only effectively decreases the stress concentration in the interface but also raises the strength of the Cu layers. This leads to the compatible strength for the 25 nm ZrCu amorphous layers and 25 nm Cu nanocrystalline layers, rendering them to deform concurrently under tension. For the ZrCu amorphous layer, the 25 nm layer thickness, equal to or smaller than the width of the shear band, was unfavorable for the formation of any major shear bands. This leads to numerous semi-homogeneous STZs dispersed within the ZrCu thin layers. With the aforementioned advantages, the reduced stress concentration at the interface and the homogeneous activation of STZs, the ZCC-25 nanolaminates could exhibit superior ductility.

In conclusion, microbridges of amorphous ZrCu film and ZrCu/Cu nanolaminates with individual layer thicknesses from 100 to 25 nm were fabricated via laser patterning, wet etching and FIB micromachining. A membrane deflection experiment was conducted to study tension deformation. The monolithic ZrCu specimen exhibited a highly brittle fracture, with poor a fracture strength of 600 MPa, low deformability and a fracture angle of 90°, and a granular structure formed as a result of the intrinsic tensile stress during film growth. The strength and deformability of the ZrCu/Cu nanolaminates increased with decreasing layer thickness. The fracture angle became close to 45° when the layer thickness decreased to 25 nm. These nanolaminates exhibited a much higher fracture strength of 2000–2500 MPa. A layer thickness of 25 nm is demonstrated to be the optimum selection for the improvement of tensile ductility in amorphous/crystalline nanolaminates.

The authors gratefully acknowledge the financial support from the National Science Council of Taiwan, ROC, under NSC 99-2811-E-110-006 and NSC 99-2818-E-110-002. The authors also gratefully acknowledge the discussion with Dr. X.H. Du of NSYSU.

[1] G. He, J. Eckert, W. Loser, L. Schultz, Nat. Mater. 2 (2003) 33–37.
[2] M.L. Lee, Y. Li, C.A. Schuh, Acta Mater. 52 (2004) 4121–4131.
[3] F.Q. Guo, S.J. Poon, G.J. Shiflet, Philos. Mag. Lett. 88 (2008) 615–622.
[4] D.C. Hofmann, J.Y. Suh, A. Wiest, G. Duan, M.L. Lind, M.D. Demetriou, W.L. Johnson, Nature 451 (2008) 1085–1090.
[5] J.W. Qiao, S. Wang, Y. Zhang, P.K. Liaw, G.L. Chen, Appl. Phys. Lett. 94 (2009).
[6] J.S.C. Jang, J.Y. Ciou, T.H. Hung, J.C. Huang, X.H. Du, Appl. Phys. Lett. 92 (2008).
[7] D.G. Pan, H.F. Zhang, A.M. Wang, Z.Q. Hu, Appl. Phys. Lett. 89 (2006).
[8] Y.K. Xu, H. Ma, J. Xu, E. Ma, Acta Mater. 53 (2005) 1857–1866.
[9] X.H. Du, J.C. Huang, K.C. Hsieh, Y.H. Lai, H.M. Chen, J.S.C. Jang, P.K. Liaw, Appl. Phys. Lett. 91 (2007).
[10] Y.H. Liu, G. Wang, R.J. Wang, D.Q. Zhao, M.X. Pan, W.H. Wang, Science 315 (2007) 1385–1388.
[11] J.R. Greer, J.T.M. De Hosson, Prog. Mater. Sci. 56 (2011) 654–724.
[12] T.G. Nieh, T.W. Barbee, J. Wadsworth, Scripta Mater. 41 (1999) 929–935.
[13] Y.M. Wang, J. Li, A.V. Hamza, T.W. Barbee, Proc. Natl. Acad. Sci. USA 104 (2007) 11155–11160.
[14] A. Donohue, F. Spaepen, R.G. Hoagland, A. Misra, Appl. Phys. Lett. 91 (2007).
[15] P.S. Ho, F. Faupel, Appl. Phys. Lett. 53 (1988) 1602–1604.
[16] F. Faupel, C.H. Yang, S.T. Chen, P.S. Ho, J. Appl. Phys. 65 (1989) 1911–1917.
[17] F. Macionczyk, W. Bruckner, J. Appl. Phys. 86 (1999) 4922–4929.
[18] Y.P. Li, G.P. Zhang, Acta Mater. 58 (2010) 3877–3887.
[19] T. Li, Z. Suo, Int. J. Solids Struct. 44 (2007) 1696–1705.
[20] R.M. Niu, G. Liu, C. Wang, G. Zhang, X.D. Ding, J. Sun, Appl. Phys. Lett. 90 (2007).
[21] J.W. Beams, Structure and Properties of Thin Films, Wiley, New York, 1959.
[22] O. Kraft, C.A. Volkert, Adv. Eng. Mater. 3 (2001) 99–110.
[23] H.D. Espinosa, B.C. Prorok, M. Fischer, J. Mech. Phys. Solids 51 (2003) 47–67.
[24] F.F. Wu, Z.F. Zhang, S.X. Mao, Acta Mater. 57 (2009) 257–266.
[25] S.G. Mayr, K. Samwer, Phys. Rev. Lett. 87 (2001).
[26] A. Misra, J.P. Hirth, R.G. Hoagland, Acta Mater. 53 (2005) 4817–4824.
[27] Y. Zhang, A.L. Greer, Appl. Phys. Lett. 89 (2006).
[28] M.Q. Jiang, W.H. Wang, L.H. Dai, Scripta Mater. 60 (2009) 1004–1007.